Science Advances
AAAS

advances.sciencemag.org/cgi/content/full/6/45/eabc9323/DC1

Supplementary Materials for

Bioinspired cilia arrays with programmable nonreciprocal motion and metachronal coordination

Xiaoguang Dong, Guo Zhan Lum, Wenqi Hu, Rongjing Zhang, Ziyu Ren, Patrick R. Onck, Metin Sitti*

*Corresponding author. Email: sitti@is.mpg.de

Published 6 November 2020, *Sci. Adv.* **6**, eabc9323 (2020)
DOI: 10.1126/sciadv.abc9323

The PDF file includes:

Other Supplementary Material for this manuscript includes the following:

(available at advances.sciencemag.org/cgi/content/full/6/45/eabc9323/DC1)

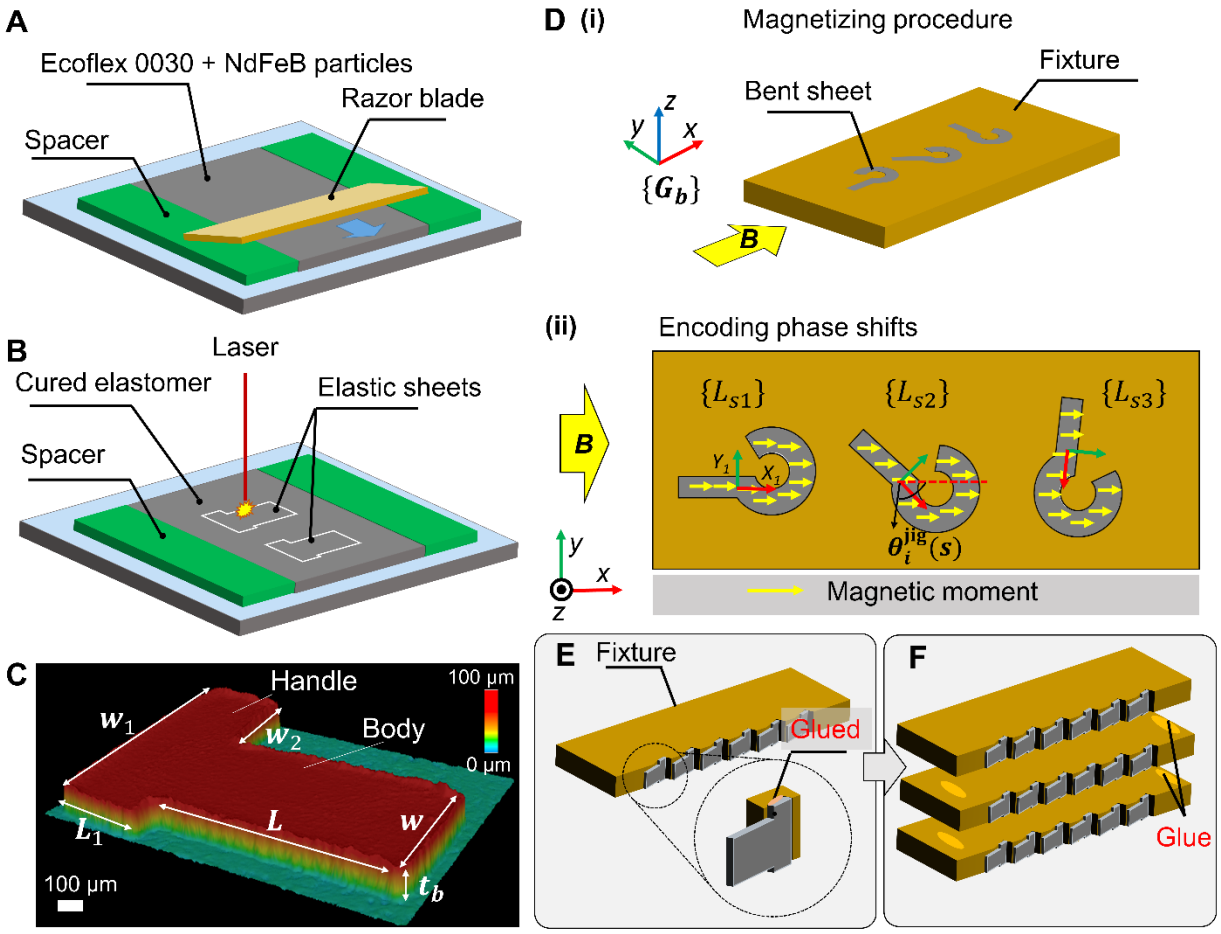

Fig. S1. Illustration of the fabrication process of an artificial cilium, its dimensions, and the assembly process of an artificial cilia array. (**A**) Illustration of the fabrication process of a ferromagnetic cilium. Mixture of Ecoflex-0030 silicone rubber and NdFeB particles (mass ratio, 1:1) are poured onto a Poly(methyl methacrylate) (PMMA) substrate with spacers to control the thickness. A single-side razor blade is used to flatten the top surface by scratching. (**B**) Illustration of cutting a cured ferromagnetic cilium using a laser machine (LPKF ProtoLaser R3, LPKF Laser & Electronics AG). (**C**) 3D laser-optical scanning image (VK-X200, Keyence Corp) of a fabricated ferromagnetic cilium with marked dimensions. A handle is designed for assembling the cilium to a fixture. (**D**) Illustration of encoding desired magnetization profiles into ferromagnetic cilia arrays. (i) Magnetizing procedure using a template jig. (ii) Illustration of obtained magnetization profiles. $\{\boldsymbol{L_{si}}\}$ $(i = 1,2,3)$: the cilium-attached coordinate systems. $\{\boldsymbol{G_b}\}$: the global coordinate system. $\theta_i^{jig}(s)$: the slope angle of the cut-out parts for i-th cilium in the magnetizing jig, denoted in $\{\boldsymbol{G_b}\}$. (**E**) Multiple cilia in a single layer bonded to an assembly fixture by gluing. (**F**) Illustration of assembling multiple layers of artificial cilia arrays by manually gluing under a stereomicroscope.

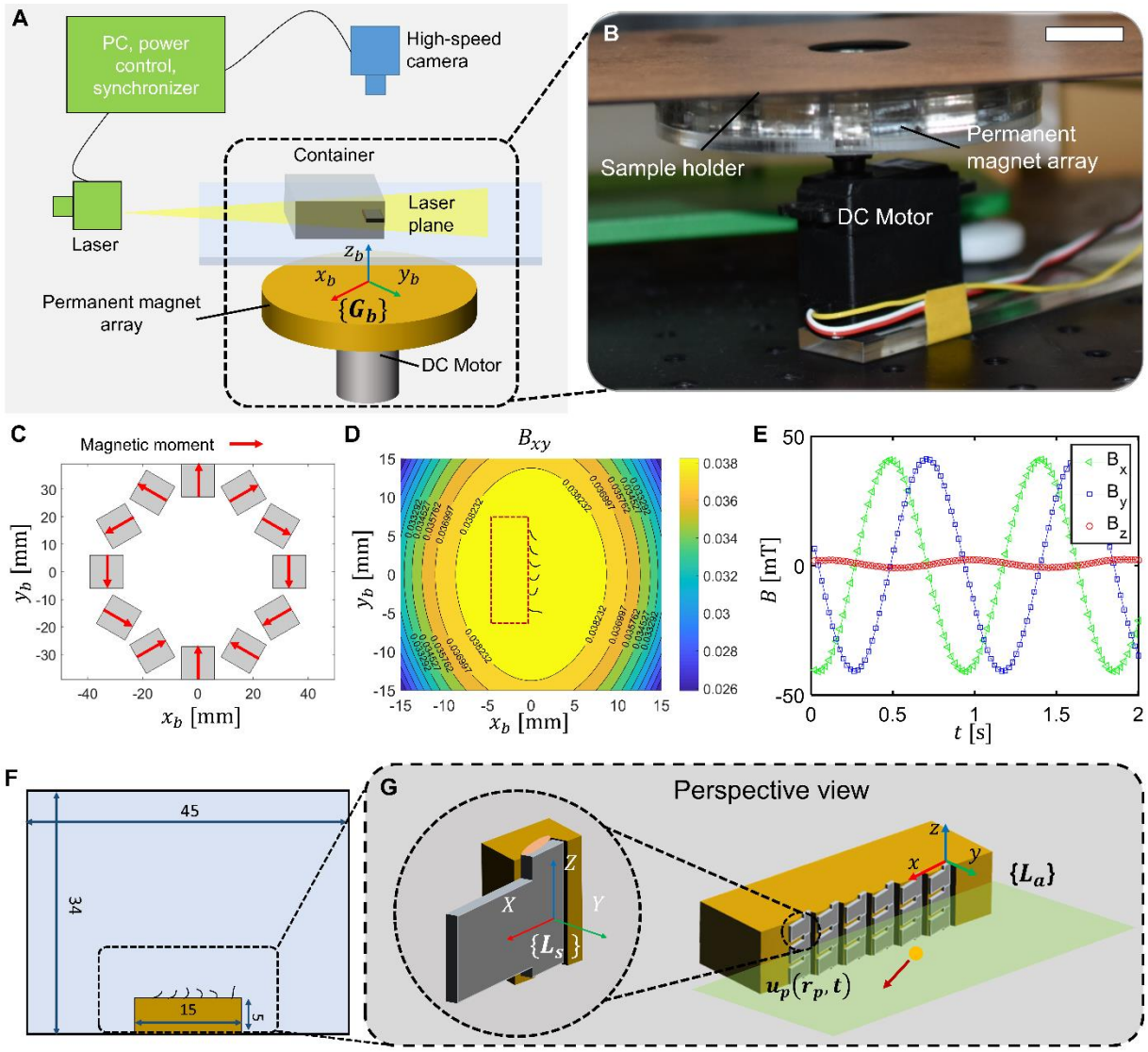

Fig. S2. Magnetic actuation and particle image velocimetry (PIV) system. (**A**) Schematics of the experimental setup. A motorized Halbach array produces a rotating $\boldsymbol{B}(t)$ (up to 60 mT). The PIV system consists of a laser, a high speed camera and a signal synchronizer. (**B**) Photo of the magnetic actuation setup. Scale bar, 2 cm. Photo credit: Xiaoguang Dong, Max Planck Institute for Intelligent Systems. (**C**) Design of the Halbach array. Each modular magnet in the array is an NdFeB magnet (N42, cubic shape, 12 mm × 12 mm × 12 mm). (**D**) Measured time-varying $\boldsymbol{B}(t)$ above the Halbach array at $x_b = 0, y_b = 0, z_b$= 15 mm in the global coordinate system $\{\boldsymbol{G_b}\}$. The *x*-*y* position of the cilia array is marked in the figure. (**E**) Simulated spatial distribution of B_{xy} within an area of 15 × 15 mm^2 on the image plane at z_b= 15 mm, using the magnetic dipole model. (**F**) Dimensions of the container (unit: mm). Container depth: 11 mm. (**G**) Illustration of the array-attached coordinate system $\{\boldsymbol{L_a}\}$ and cilium-attached coordinate systems $\{\boldsymbol{L_s}\}$ in a perspective view. Yellow dot: a tracer particle in the fluid. Red arrow: the instant velocity $\boldsymbol{u_p}(\boldsymbol{r_p}, t)$ of a tracer particle at position $\boldsymbol{r_p}$ at time *t* denoted in $\{\boldsymbol{L_a}\}$.

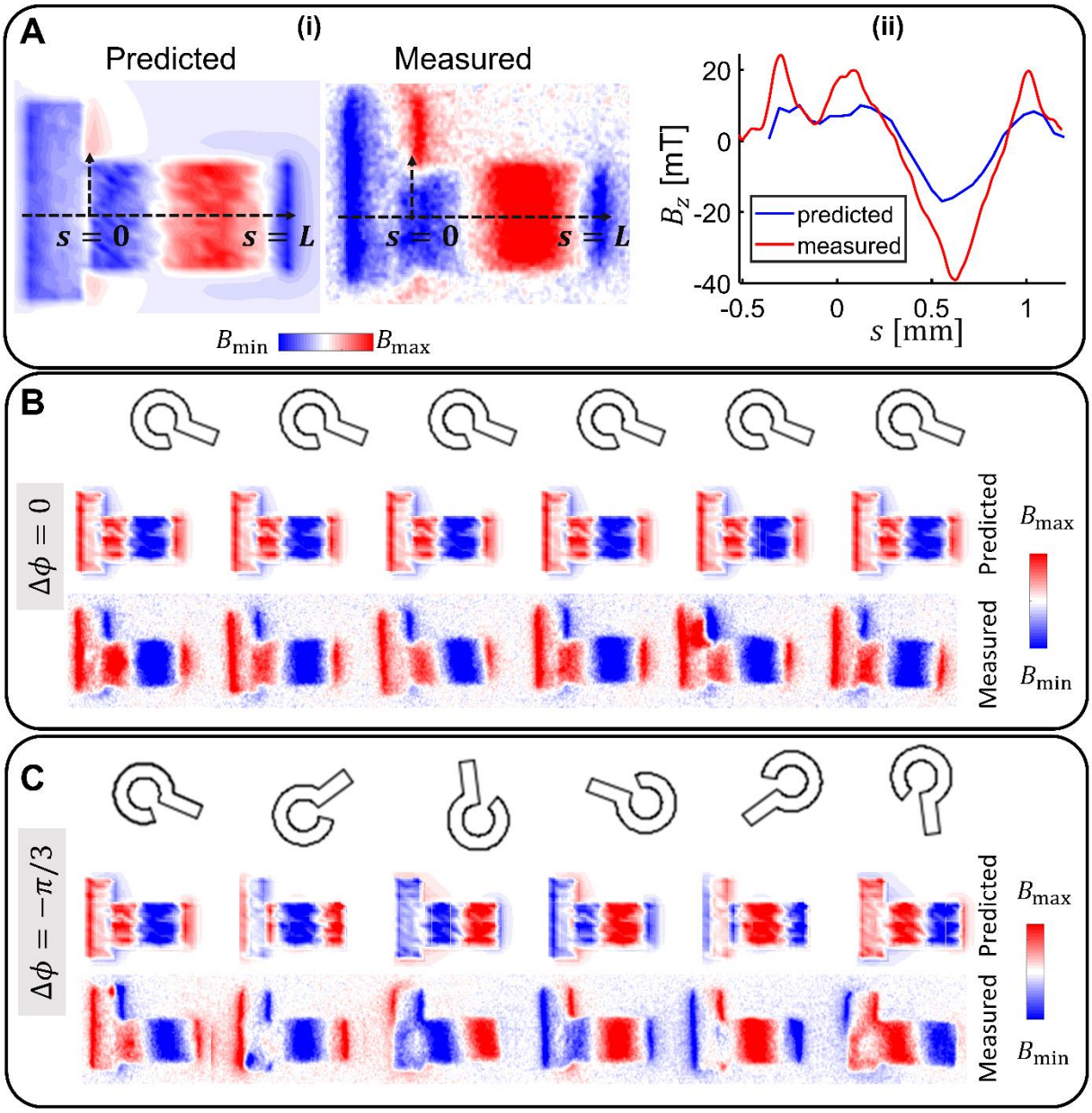

Fig. S3. Characterization of the programmed magnetization profiles. (**A**) Comparing predicted and measured B_z produced by a magnetized cilium at its surface. (i) Comparison of B_z produced at the bottom surface. (ii) Comparison of B_z along a marked line at the bottom surface. The magnetic field produced by a magnetized cilium is measured by a 2D magneto-optical sensor (MagView S, Matesy GmbH). The predicted B_z is given by dividing the cilium into multiple voxels and approximating the magnetic field of each voxel using the magnetic dipole model. (**B**) Template jigs for magnetizing artificial cilia and the corresponding optical-magnetic images of ferromagnetic cilia with a phase shift $\Delta\phi = 0$. (**C**) Template jigs for magnetizing artificial cilia and the corresponding optical-magnetic images of ferromagnetic cilia with a phase shift $\Delta\phi = -\pi/3$. In the color bars, $B_{\min} = -20$ mT, $B_{\max} = 20$ mT.

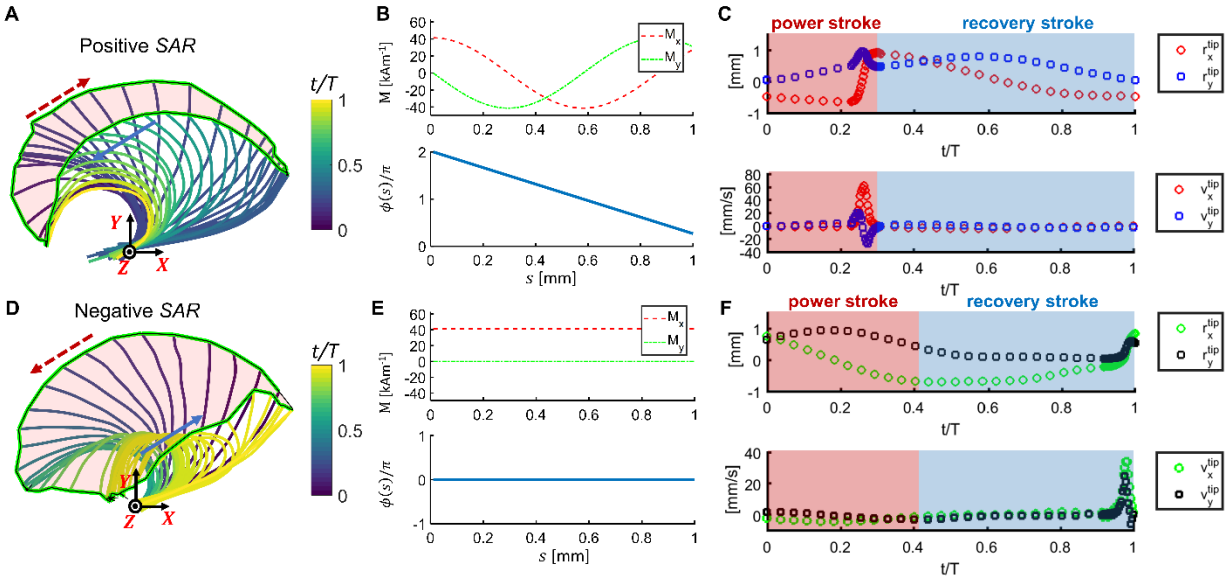

Fig. S4. Two typical nonreciprocal artificial cilium dynamics in experiments. (**A**) Single cilium dynamics with a positive SAR. (**B**) The magnetization profile of the cilium in (**A**). $\phi(s) = -\frac{3\pi}{8} + 1.75\pi(\frac{s}{L})$. $M(s)$ = 40 kA·m^{-1}. (**C**) The tip position and velocity in a whole period of the cilium in (**B**). (**D**) Single cilium dynamics with a negative SAR. (**E**) The magnetization profile of the cilium in (**D**). $\phi(s) = -\frac{7\pi}{8}$. $M(s)$ = 40 kA·m^{-1}. (**F**) Tip position and velocity in a whole period of the cilium in (**E**). In (**B**) and (**E**), the color of the cilium indicates the timing within a beating period. In (**A**) and (**B**), the red and blue arrows indicate the directions of cilium tips in the power and recovery strokes, respectively. $\boldsymbol{B}(t)$: f = 2.5 Hz, B_m = 40 mT.

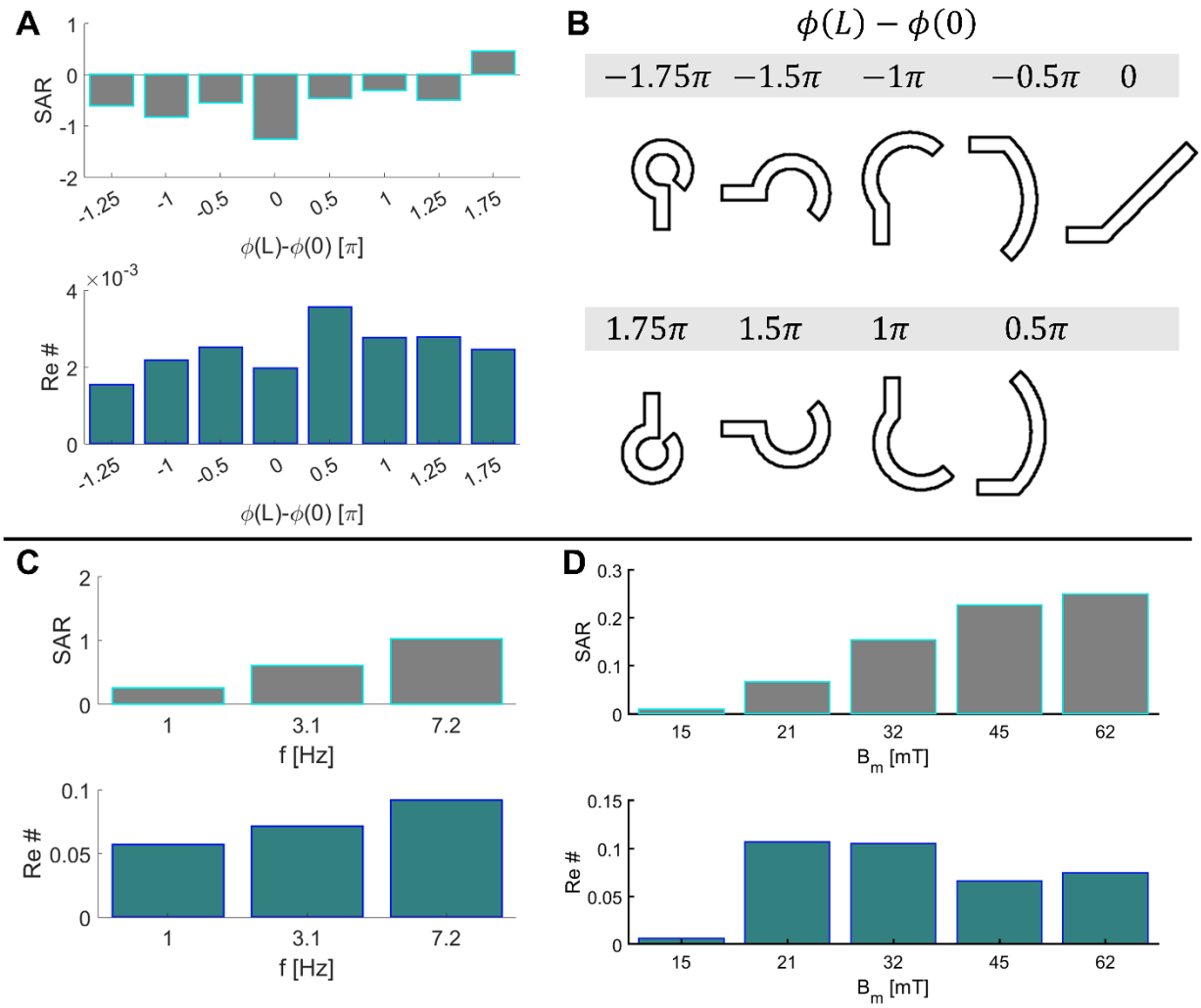

Fig. S5. Swiping area ratio (SAR) and maximal local Reynolds number (*Re*). (**A**) SAR (defined in the main text) and maximal local *Re* as functions of magnetization phase profiles. $\boldsymbol{B}(t)$: $f = 2.5$ Hz, $B_m = 38$ mT. (**B**) Magnetizing jigs for ferromagnetic cilia with different $\phi(0) - \phi(L)$ in (**A**). (**C**) SAR and maximal local *Re* as functions of the actuation frequency of $\boldsymbol{B}(t)$. $\phi(s) = \left(1 - \frac{s}{L}\right) 1.75\pi$. $B_m = 38$ mT. (**D**) SAR and maximal local *Re* as functions of the magnitude of $\boldsymbol{B}(t)$. $\phi(s) = \left(1 - \frac{s}{L}\right) 1.75\pi$. $f = 2.5$ Hz. In all experiments, the local *Re* is calculated using the formula $Re = |\boldsymbol{u}_{\text{noslip}}(s,t)| w \rho_f \cdot \mu_f^{-1}$. $\boldsymbol{u}_{\text{noslip}}(s,t)$ is the instant velocity of the cilium at different segments extracted from videos taken by a high-speed camera. w is the width of the cilium. ρ_f and μ_f are the density and dynamic viscosity of the fluid, respectively. The dimensions of the cilia are $L = 1$ mm, $w = 550$ μm, $t_b = 100$ μm. Glycerol (dynamic viscosity: 0.876 Pa·s) is used in all experiments.

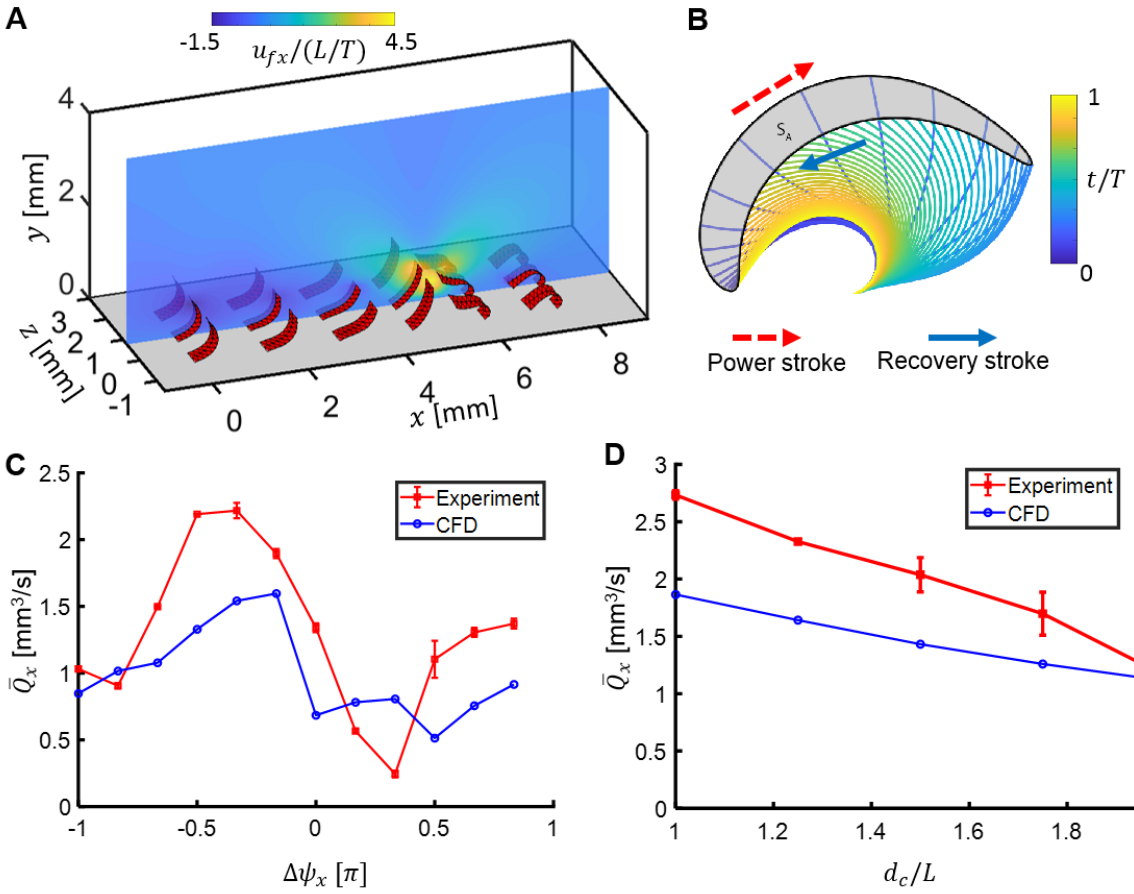

Fig. S6. Computational fluid dynamics (CFD) simulation in comparison with experimental data. (**A**) Snapshot of the CFD simulation for an artificial cilia array of a symplectic metachronal wave ($\Delta\psi_x = \frac{\pi}{6}$). The colors represent the fluid flow velocity in the x-direction (scaled by L/T). $L = 1$ mm, $T = 1\ s$. (**B**) Simulated beating kinematics of a single cilium. The colored curves represent the time-varying shapes of the cilium within a beating cycle T. The grey-shaded area represents the swiping area (S_A) of the cilium tip within T. $B_m = 38$ mT, $T = 1\ s$. (**C**) The average volume flow rate $\bar{Q}_x(x_0) = \Delta z \int_{y_0}^{y_0+\Delta y} \bar{u}_{fx}(x_0, y)\, dy$ as a function of different phase shifts $\Delta\phi/\pi$ ($d_c = 1.5L$) in the experiment and CFD simulation. $\Delta z = 3w$, $\Delta y = 3L$, $x_0 = 0.5(x_{c3} + x_{c4})$. (**D**) The average volume flow rate $\bar{Q}_x(x_0)$ as a function of cilia spacing d_c/L ($\Delta\psi_x = -\frac{\pi}{3}$) in the experiment and CFD simulation.

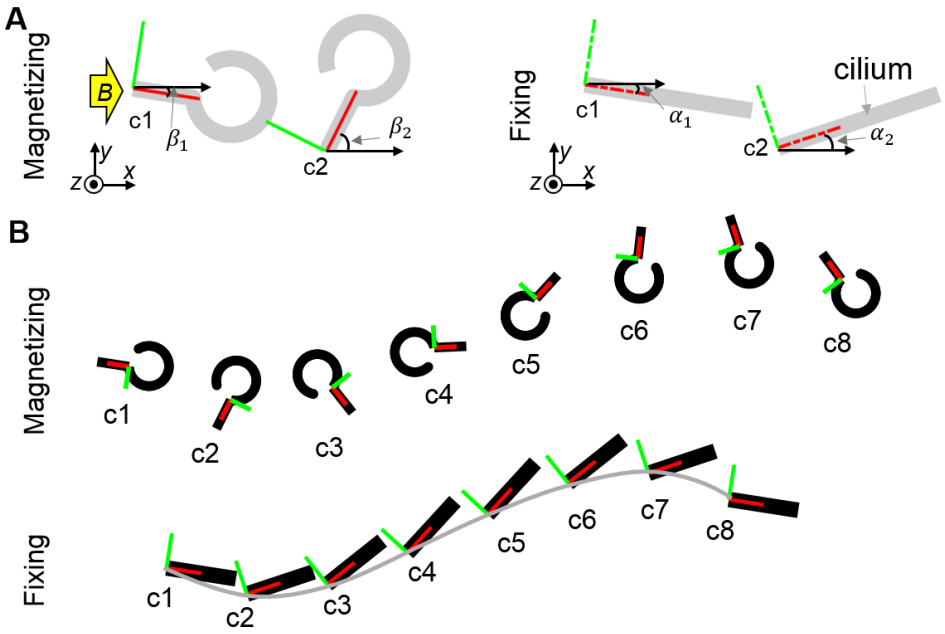

Fig. S7. Design of artificial cilia arrays to produce metachronal waves on curved surfaces. (**A**) Illustration of the method to program the magnetization profiles for compensating the rotation angles on curved surfaces. The design rule is given by $\beta_2 - \beta_1 = \Delta\phi + \alpha_2 - \alpha_1$. (**B**) The magnetizing and fixing jigs for creating an artificial cilia array on a curved surface.

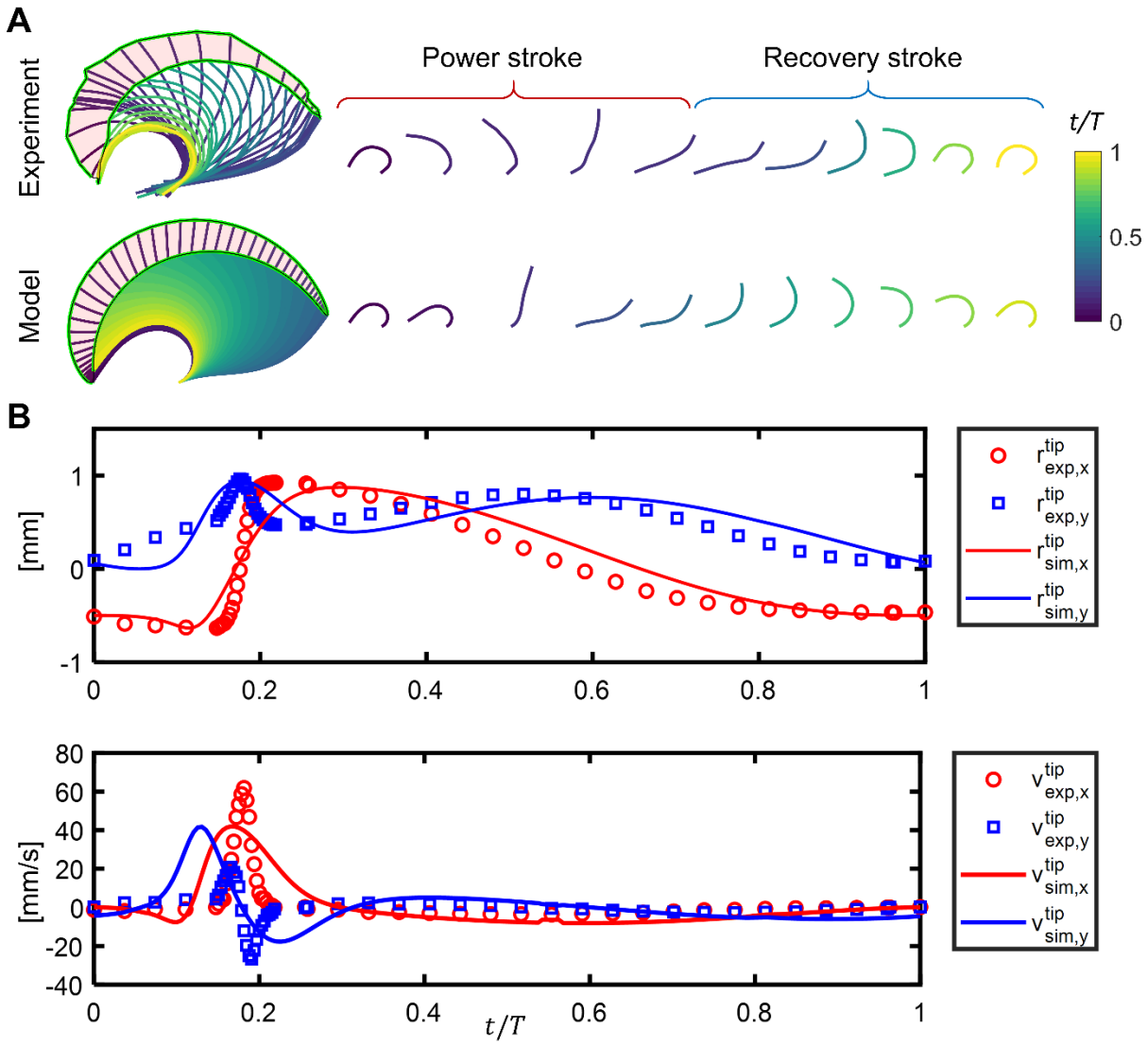

Fig. S8. Comparison of experimental and model-predicted single cilium dynamics. (**A**) Comparison of the overall dynamics. (**B**) Comparison of the displacement and velocity of the cilium tip. $\boldsymbol{B}(t)$: f = 2.5 Hz, B_m = 40 mT.

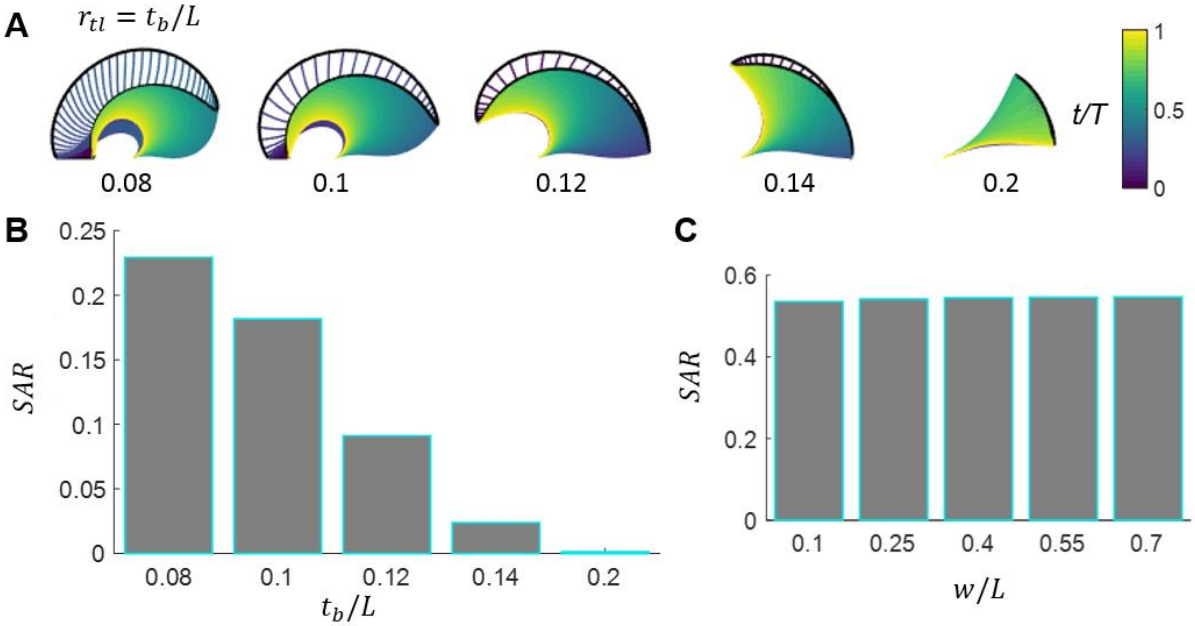

Fig. S9. Swiping area ratio (SAR) as a function of the artificial cilium dimensions based on numerical simulations. (**A**) Simulated dynamics for an artificial cilium with different thickness-to-length ratios ($r_{tl} = t_b/L$). (**B**) SAR as a function of r_{tl}, while keeping the width-to-length ratio ($r_{wl} = w/L$) as 0.6. (**C**) *SAR* as a function of r_{wl}, while keeping $r_{tl} = 0.12$. In all simulations, for $\boldsymbol{B}(t)$: f = 2.5 Hz, B_m = 40 mT.

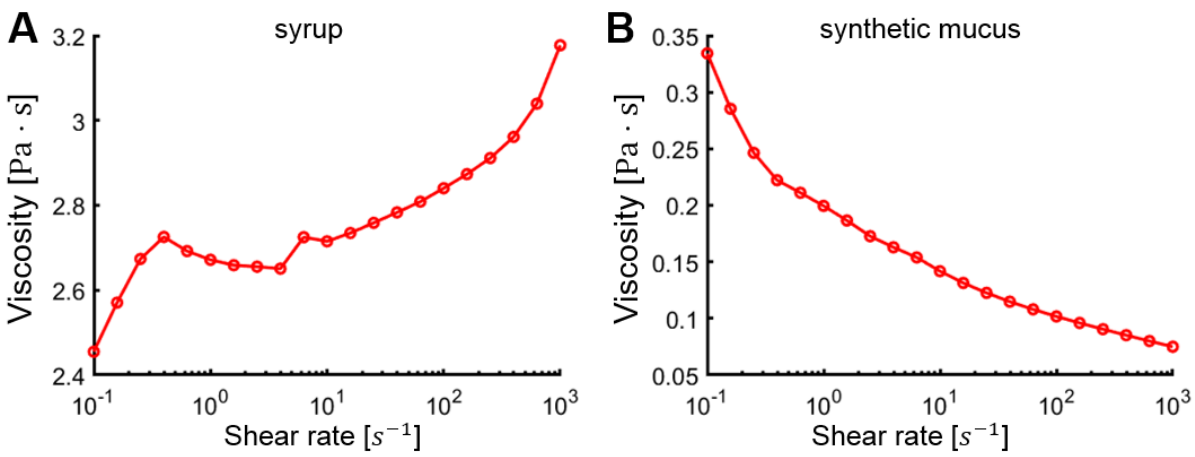

Fig. S10. Rheology properties of syrup and synthetic mucus used in the experiments. (**A**) Dynamic viscosity of syrup as a function of the shear rate. (**B**) Dynamic viscosity of synthetic mucus as a function of the shear rate. The rheology test is carried out in a Discovery HR-2 rheometer (TA Instruments, Inc.).

Table S1. Comparison of the fluid pumping performance at low *Re* (< 0.1) with literature.

Literature	Scaled fluid velocity $v_{\text{scaled}} = \bar{v}_x/(Lf)$	Fluid velocity $\bar{v}_x$	Cilia length L	Actuation frequency f	*Re*
(28)	0.0091	8 μm/s	25 μm	34 Hz	0.025
(29)	0.1	3.3 μm/s	31 μm	1 Hz	<0.01
(33)	0.25	83 μm/s	4 mm	0.083 Hz	0.002 **
This work	**0.38**	0.95 mm/s	1 mm	2.5 Hz	0.03

** Estimated value.

Supplementary Note 1. Calculation of energy efficiency in fluid propulsion

Within each beating cycle, the input energy of the system originates from the work done by the magnetic torque on each cilium. The average variance of the kinetic energy and elastic energy in a full beating cycle is nearly zero at a steady beating state. We use the energy efficiency ϵ_c in a dimensionless form proposed in (12) to quantify the energy efficiency in fluid propulsion. ϵ_c is defined as the ratio of the energy consumption of cilia per unit time and the required power to get the same average fluid flow velocity by a constant driving-force density in a semi-infinite system (12), which is given by:

$$\epsilon_c = \frac{16}{3L}\frac{\bar{v}_x^2 \mu_f A}{P_{\text{in}}}, \tag{1}$$

where $\bar{v}_x$ is the average fluid flow velocity in the $+x$ direction near the cilia surface, μ_f is the dynamic viscosity of the fluid, $A = (N-1)d_c \cdot w$ is a selected area in the x-z plane, and P_{in} is the average input power of all N cilia in the array within a beating cycle. P_{in} is obtained in numerical simulation by integrating the work done by the distributed magnetic torque in unite time as,

$$P_{\text{in}} = \frac{N}{T}\int_0^T \int_0^L \tau_m(s,t) \cdot \frac{\mathrm{d}\theta}{\mathrm{d}t}\,\mathrm{d}s\,\mathrm{d}t\,. \tag{2}$$

We investigated the artificial cilia array with different phase shifts and inter-cilium spacing in Fig. 2B,C. The results of approximated energy efficiency are shown in Fig. S11 for artificial cilia arrays with different phase shifts and inter-cilium spacing. The best case is about 0.46% when $\Delta\psi_x = -\frac{\pi}{3}$ and $d_c = L$. It should be noted that the energy efficiency results are only an approximation. Other energy efficiency metrics (10,13) could also be used, which may result in different quantities of energy efficiency. A more precise quantification of the energy efficiency requires better modeling of the output energy into the fluids, which will be studied in the future.

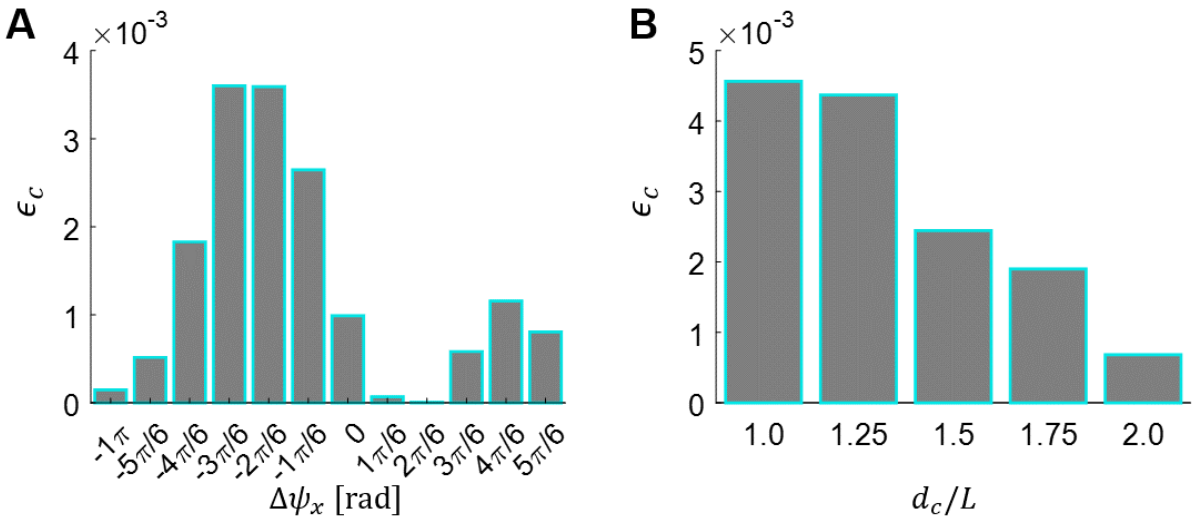

Fig. S11. Energy efficiency of fluid propulsion by different artificial cilia arrays. (**A**) Energy efficiency as a function of phase shifts. The inter-cilium spacing is $d_c = 1.5L$. (**B**) Energy efficiency as a function of the inter-cilium spacing. The energy efficiency ϵ_c is defined in Eqn. (1). The average fluid flow velocities by the investigated artificial cilia arrays were obtained from the experimental results in Fig. 2. The applied magnetic actuation fields have f = 2.5 Hz and B_m = 40 mT in both the experiments of obtaining the average fluid flow velocities and the numerical simulation of estimating the energy input.

Notes for movies S1-S7

Notes: The viscous fluids in all supplementary videos are glycerol (dynamic viscosity: 0.876 Pa·s) if not explicitly mentioned.

Movie S1. **Dynamics of single artificial cilia and 1D metachronal waves of artificial cilia arrays.** This video first shows single artificial cilia beating in glycerol with a positive and negative swiping area. It also shows an artificial cilia array with a 1D metachronal wave of an arbitrary phase shift e.g. $\Delta\psi = -\frac{\pi}{3}$. The yellow arrows indicate the distribution of fluid flow velocity.

Movie S2. 2D metachronal waves propagating on an artificial cilia carpet. This video shows the ability of encoding arbitrary 2D metachronal wave into a six by six artificial cilia array. It also shows such a cilia array can transport particles in viscous fluids at low *Re* (~0.03). The phase shifts in +*x* and +*z* direction are $\Delta\psi_x = \Delta\psi_z = -\frac{\pi}{3}$.

Movie S3. Comparing performance of pumping viscous fluid flow by different metachronal coordination. This video shows the superior transportation of artificial cilia arrays with antiplectic waves by comparing particle transportation performance. 1D artificial cilia arrays with phase shifts including $\Delta\psi_x = -\frac{\pi}{3}$, $\Delta\psi_x = 0$, and $\Delta\psi_x = \frac{\pi}{3}$ are presented for cases with positive and negative swiping areas.

Movie S4. Bioinspired cilia arrays with optimal metachronal waves propagating on curved surfaces. This video shows bio-inspired cilia arrays with optimal metachronal waves propagating on curved surfaces, as well as their ability of transporting particles efficiently at low *Re* using the optimal metachronal coordination. It first shows circular surface and then an "S"-shaped surface. Comparison of particle transportation by metachronal coordination on curved surfaces is presented.

Movie S5. Tubal transportation of viscous fluids by artificial cilia with optimal metachronal coordination. This video shows efficient transportation of particles in a narrow channel filled with viscous fluids (glycerol, syrup and synthetic mucus), by designing the optimal metachronal coordination of two artificial cilia arrays. Pumping performance of two artificial cilia arrays with jointly designed metachronal coordination has been compared with that of only the top or bottom artificial cilia array.

Movie S6. Efficient mixing of viscous fluids by artificial cilia with optimal coordination. This video shows rapid and complete mixing of viscous fluids (at low $Re < 0.03$) visualized by the dye by designing the optimal metachronal coordination of two artificial cilia arrays.

Movie S7. Pumping and imaging biofluids in enclosed channels. This video shows wireless actuating and non-invasive imaging of artificial cilia arrays to pump fluids including water and mouse blood in enclosed channels. Color Doppler ultrasound imaging was used to measure the fluid speed while pumping the mouse blood.